Aspects of normal-state resistivity of the cuprate superconductors $Bi_2Sr_2CuO_{6+x}$, $Tl_2Ba_2CuO_{6+x}$, and $HgBa_2CuO_{4+x}$

Samantha Shears,[*] Michael Arciniaga,[†] and B. Sriram Shastry[‡]
Physics Department, University of California, Santa Cruz, California 95064, USA

(Received 7 February 2025; revised 29 April 2025; accepted 22 May 2025; published 20 June 2025)

Planar normal-state resistivity data from three families of hole-doped single-layer cuprate superconductors, i.e., Bi2201 ($Bi_2Sr_2CuO_{6+x}$), Tl2201 ($Tl_2Ba_2CuO_{6+x}$), and Hg1201 ($HgBa_2CuO_{4+x}$), are calculated using the extremely correlated Fermi liquid theory (ECFL). This theory was recently employed by us to compute the resistivity of three families of single-layer cuprate superconductors, i.e., $La_{2-x}Sr_xCuO_4$ (LSCO), $Bi_2Sr_{2-x}La_xCuO_{6+\delta}$ (BSLCO), and $Nd_{2-x}Ce_xCuO_4$ (NCCO), followed by a detailed comparison. Adding the three systems studied here accounts for *all* the remaining single-layer compounds, where data are available for a range of densities and temperatures, thereby providing a comprehensive study of one class of important cuprate superconductors. The added study of the material Bi2201 is of particular interest since it is the system where the almost linear in temperature resistivity was first reported in 1990. Only recently, in 2022, has a systematic doping analysis become available. The Tl2201 system has two distinct sets of band parameters that fit the same Fermi surface, providing new challenges and insights into the ECFL theory.

DOI: 10.1103/89cj-5qhs

I. INTRODUCTION

Strongly correlated systems such as high-T_c systems provide a formidable challenge to our current understanding of the physics of interacting Fermi systems. The standard framework is largely built using the density functional theory of Kohn *et al.*, supplemented by methods incorporating weak- or moderate-strength interactions. New techniques to calculate the physics of strongly correlated systems, where interactions are much bigger than the band energy, are few and their reliability is not fully established. A major question that remains to be settled is whether such strongly correlated systems are Fermi liquids or some variety of non-Fermi liquids. Monitoring and interpreting the behavior of the resistivity in the normal state can, in principle, identify the nature of the underlying normal state and distinguish between Fermi liquids and non-Fermi liquids. Experimental data on many systems show a complex set of T dependences in different regimes, varying with the density, and understanding them from the theoretical viewpoint is our main task.

The extremely correlated Fermi liquid theory (ECFL) [1] was developed starting in 2011, to extend the theory of resistivity due to inelastic electron-electron scattering. This important mechanism was first suggested by Landau and Pomeranchuk [2] in 1937. They noted that electron-electron scattering would lead to a T^2 contribution to the resistivity of simple metals and, on adding the phonon scattering contribution, give rise to a $\rho \sim \alpha T^2 + \beta T^5$ behavior at low temperatures. The key point made in [2] is that in a simple metal with electrons moving in a Bloch band, the conservation of the total momentum of a pair of electrons in the scattering process does not imply the conservation of their total *velocity*. In the presence of the lattice, the conserved object is the "crystal momentum," i.e., momentum modulo a reciprocal lattice vector, and the velocity refers to the group velocity of the electron waves. This feature allows a certain fraction of the scattering processes—the *umklapp* processes—with a nonzero reciprocal lattice vector to balance the momentum, while allowing a nonzero transfer of velocity, leading to a nonvanishing resistivity. This is true even in the case of a single band of electrons, while adding other bands makes this easier. For simple metals, the magnitude of the umklapp contribution was quantitatively estimated in 1972 [3]. In metals with stronger interactions—such as transition metals and heavy Fermi systems [4,5]—the umklapp fraction is estimated to be close to unity. While strongly correlated metals are experimentally very important and widespread in occurrence, their theoretical treatment using controlled methods is a highly challenging problem. The usual method of using the interaction strength as a perturbative parameter is clearly undermined if it is very large, even bigger than the band width, and resorting to summation of diagrams, etc. becomes very dubious. This has created a large theoretical gap in the space of techniques, wherein the ECFL theory was launched in 2011 [1]. The ECFL theory yields, for strongly correlated systems, a resistivity as a function of the basic material parameters including the band parameters, density, the interaction constants, etc. [see Eq. (8)]. At low T and for densities close to half filling, the Landau-Pomerantschuk resistivity $\rho \sim T^2$ is replaced by a complex behavior, with $\rho \sim T^2$ at very low T crossing over to a linear, i.e., $\rho \sim T$, behavior. The crossover temperature is remarkably low for most parameters, as a consequence of strong correlations and the proximity to a Mott-Hubbard insulating state.

[*]Contact author: sshears@.ucsc.edu
[†]Contact author: michael.arciniaga@gmail.com
[‡]Contact author: sriram@physics.ucsc.edu

The ECFL theory is currently formulated for systems that can be described by a single correlated band. The interactions can be modeled by the large Hubbard-U model or the closely related t-J model. The ECFL theory is able to provide quantitative results for the resistivity, using the following ingredients:

(i) A single copper oxide with dimensionless band parameters $t'/t, t''/t \ldots$ retrieved from the shape of the Fermi surface determined by angle-resolved photoemission spectroscopy (ARPES). Here the interlayer hopping is assumed to be negligible.

(ii) The particle density n (the number of electrons per copper), usually obtainable from the Luttinger-Ward area of the Fermi surface found from ARPES.

(iii) The interlayer lattice constant c_0 obtainable from crystallography—it is usually half the c-axis lattice constant c_L in the almost tetragonal unit cell.

These items determine all parameters in the t-J model given by Eq. (1), with the exception of J and t itself. Our earlier results suggest that J is not a sensitive parameter [6] and we take $J/t \sim 0.17$ in most of our work. The value of t is the single adjustable parameter that is fixed for each family of materials studied, by choosing a reasonable overall fit to the resistivity over many densities. Having access to data sets containing several densities is advantageous; with an overall fit, one can expect to reduce the implicit bias in the fits if only a single density is considered. It should be noted that the results of the ECFL [see Eqs. (5) and (12)] can be broadly characterized as leading to a resistivity that is quadratic in temperature below a surprisingly low scale (given the large $t \sim 1$ eV), which crosses over to an almost linear behavior over a wide temperature window, often termed as the 'strange metal' regime, and finally with slight curvature reappearing at fairly high T ($\sim$600 K). The quasiparticle weight turns out to be much reduced from unity, and the crossover T scales are sensitively dependent on the density and band parameters $t'/t, t''/t \ldots$. The detailed equations of the ECFL theory given in [1,7], and summarized below, produce this complex variety of behavior starting from the microscopic parameters defining the model given by Eq. (1).

In a recent paper [7], we applied the ECFL to four major families of cuprate superconductors—$La_{2-x}Sr_xCuO_4$ (LSCO) [8], $Bi_2Sr_{2-x}La_xCuO_{6+\delta}$ (BSLCO) [8], $Nd_{2-x}Ce_xCuO_4$ (NCCO) [9] and $La_{2-x}Ce_xCuO_4$ (LCCO) [10]—where all of the above ingredients are present. These systems are characterized by a single sheeted Fermi surface and with single-layer (i.e., well-separated) copper oxide planes, that allow a quasi-two-dimensional theory to be applied. It is shown in that paper that theory shows quantitative agreements with experiments over several densities. For LSCO, we studied samples at 11 densities, and for BSLCO, we studied samples at seven densities. For the electron-doped materials, i.e., NCCO and LCCO, we studied the two available metallic samples and we studied samples at four densities, respectively. The temperature range of most of the systems was from T_c up to 300 and 400 K in the case of LSCO. For most cases, Ref. [7] reports a close agreement between theory and experiment.

The present study takes the goals of [7] forward, by including three other systems and thus providing a comparison between the ECFL theory and experiment for *all* single-layered cuprates known so far. For this purpose, we study the following compounds here. The single-layer system Bi2201 was omitted from our study in [7] since results were available for only a single density at that time [11,12], and is included in this work since further data have been published meanwhile [13]. This system was experimentally studied in a few influential papers [11,12] in 1989 and 1990. In these papers, the T-linearity of resistivity was reported over a remarkably large range of T, between 8 and $\sim$800 K. This result was expected to be a harbinger of universal T-linearity of resistivity in the cuprates, therefore possibly implying the general demise of any kind of Fermi liquid theory in these systems. However, the reported results were confined to a single composition, and hence some of the ingredients mentioned above were missing. The situation remained unchanged for almost three decades, until very recently. This system has been studied recently in [13], who have reported data on a few different densities overlapping with that in [11,12], albeit over a smaller temperature range of $T \lesssim 300$ K.

New results on another interesting single-layer system Tl2201 at a set of densities have also been reported recently in [14–16]. This system is of additional interest since it allows convenient access to the highly overdoped regime. The present work extends the earlier work [7] to include parameters relevant to the available samples of Bi2201 and Tl2201.

We mention that Tl2201 leads to an interesting and unexpected theoretical situation, i.e., we found that the reported Fermi surface can be fit with a significantly different set of band parameters from the ones reported in [15,16], and we are able to nontrivially test a theoretical hypothesis that it is the shape of the Fermi surface—rather than the values of the band parameters—that determines the computed resistivity. For context, we note that in the t-J model, the hopping parameters multiply the (Gutzwiller) correlated Fermi operators, which can be viewed as consisting of four fermions, and hence this hypothesis seems to require testing.

Finally, we present the results of study of the system Hg1201 [17–22]. This system, together with the two compounds listed above and the four compounds in [7], completes the known list of single-layer cuprates.

A. The t-J model and the ECFL methodology

The t-J model [23] is very important for understanding strongly correlated systems. This model is related to the Hubbard model in the $U \to \infty$ limit, precluding double occupancy. The model is written in the usual form,

$$H = P_G H_{tb} P_G + J \sum_{\langle i,j \rangle} \left(\vec{S}_i . \vec{S}_j - \frac{1}{4} n_i n_j \right), \tag{1}$$

where the first term is the Gutzwiller projected band energy, i.e., P_G is the Gutzwiller projector, and the exchange term is restricted to nearest neighbors. The tight-binding term is written as a sum over a range of neighbors, where $\vec{r}_i \to i$ are the locations of the lattice sites assumed to be on a square lattice with lattice constant a_0, and with

$$H_{tb} = -\sum_{ij} t_{ij} C^\dagger_{i\sigma} C_{j\sigma} = \sum_{k\sigma} \varepsilon_k C^\dagger_{k\sigma} C_{k\sigma} \tag{2}$$

with

$$-t_{ij} = -t\delta_{|i-j|=a_0} - t'\delta_{|i-j|=\sqrt{2}a_0} - t''\delta_{|i-j|=2a_0}, \quad (3)$$

and the Fourier transform of $-t_{ij}$ is the band dispersion $\varepsilon(\vec{k})$ given by

$$\varepsilon(\vec{k}) = -2t[\cos(k_x a_0) + \cos(k_y a_0)] - 4t'\cos(k_x a_0)\cos(k_y a_0) - 2t''[\cos(2k_x a_0) + \cos(2k_y a_0)]. \quad (4)$$

Details of the ECFL formalism have been extensively discussed in prior papers [1], and also in the resistivity related paper [7]. Here we will provide the barest overview to familiarize the reader with notations.

In ECFL, a one-electron Green's function can be broken into the product of an auxiliary Green's function **g** and the caparison function $\tilde{\mu}$,

$$G(\vec{k}, i\omega_n) = \mathbf{g}(\vec{k}, i\omega_n) \times \tilde{\mu}(\vec{k}, i\omega_n), \quad (5)$$

where $\omega_n = \frac{2\pi}{\beta}(n + \frac{1}{2})$ is the fermionic Matsubara frequency and $\mathbf{g}(\vec{k}, i\omega_n)$ is a canonical fermion propagator. $\tilde{\mu}$ and **g** are found from two self-energies $\Psi(\vec{k}, i\omega_n)$ and $\chi(\vec{k}, i\omega_n)$:

$$\tilde{\mu}(\vec{k}, i\omega_n) = 1 - \lambda\frac{n}{2} + \lambda\Psi(\vec{k}, i\omega_n),$$
$$\mathbf{g}(\vec{k}, i\omega_n)^{-1} = i\omega_n + \mu' - \tilde{\mu}(\vec{k}, i\omega_n)[\varepsilon(\vec{k}) - u_0/2] - \lambda\chi(\vec{k}, i\omega_n), \quad (6)$$

where λ is an interpolation parameter set equal to 1 at the end, $\mu' = \mu - \frac{1}{2}u_0 + \lambda nJ$, and u_0 is a Lagrange multiplier, which, along with the thermodynamic chemical potential μ, is fixed from two particle-number sum rules,

$$n_G = 2\Sigma_k G(k)e^{i\omega_n 0^+} = n,$$
$$n_g = 2\Sigma_k \mathbf{g}(k)e^{i\omega_n 0^+} = n. \quad (7)$$

In the ECFL theory, the two self-energies satisfy coupled integral equations that are available as an expansion in powers of λ; this is truncated to second order for this problem, as in [7]. We note that $\lambda = 0$ gives the noninteracting theory, whereas the exact Gutzwiller projected theory requires a summation of the λ expansion to all orders. By truncating the expansion to second order, we are making an approximation to the exact theory, which captures some of the significant effects of strong correlations, as argued in [1,7]. Solving the equation gives the spectral function $A(\vec{k}, \omega)$ found by analytically continuing to real frequencies from the Matsubara frequencies $i\omega_n \to \omega + i0^+$ by using $A(\vec{k}, \omega) = -\frac{1}{\pi}\mathrm{Im}G(\vec{k}, \omega)$.

B. Formulation for resistivity

Within the ECFL theory, we express the resistivity as

$$\rho = R_{vK} \times c_0 \times \bar{\rho}\left(\frac{t'}{t}, \frac{t''}{t}, \frac{k_B T}{t}, \frac{J}{t}, n\right), \quad (8)$$

where $R_{vK} = \frac{h}{e^2} = 25813\Omega$ is the von Klitzing resistance, n is the particle density, and c_0 is the interlayer separation for the cuprates—equaling half the c-axis lattice constant c_L for the single-layer compounds considered here. Here, $\bar{\rho}$ is the dimensionless resistivity computed in terms of the microscopic model parameters and temperature measured in units of t. We express $\bar{\rho}$ in terms of the band velocities $\vec{v}_{\vec{k}} = \vec{\partial}_{\vec{k}}\varepsilon_k$, the Fermi function $f(\omega) = \{e^{\beta\omega} + 1\}^{-1}$, and the electron spectral function $A(\vec{k}, \omega)$ obtained from the ECFL formalism [1] as

$$\frac{1}{\bar{\rho}} = \frac{(2\pi)^2}{a_0^2}\int_{-\infty}^{\infty} d\omega(-\frac{\partial f(\omega)}{\partial\omega})\langle A^2(\vec{k}, \omega)\left(\hbar v_k^x\right)^2\rangle_{\vec{k}}. \quad (9)$$

The behavior of $\bar{\rho}$ is quite intricate and is discussed below as a function of various parameters.

For typical parameters encountered in our study, the resistivity ρ is found to be linear in T in a certain range of temperature, wherein one can express it in a Drude-type form $\rho = \frac{m_*}{n_* e^2\tau}$, where the relaxation time $\tau = \frac{h}{k_B T}$ involves only Planck's constant. This is sometimes referred to as the "Planckian limit" [16], which is free from any material specific scale. Taking this observation as seriously suggesting a universal and otherwise scale-free physics seems hard. It is impossible to extract τ from experiments, unencumbered by other essential parameters such as n_*, m_*. The parameters n_*, m_* in such a fit can be determined in each case and are far from being invariant—they vary with all other basic parameters of the theory. A similarly nonuniversal situation seems to occur in most experiments as well, where specific sets of data show a linear-in-T behavior over a restricted range.

C. Computation

For Tl2201 and Bi2201, the ECFL equations were solved iteratively on four $N_k \times N_k$ lattices with $N_k = 81$, 86, 91, and 96, with a frequency grid of $N_\omega = 2^{14}$ points. In [7], smaller systems, $N_k = 62$, were studied, but otherwise we used the identical computational procedure. Even at these larger sizes, our systems are still too small to display the systematics expected from finite-size scaling analysis. The different studied sizes show small but unsystematic variations. These are treated by averaging the resistivity results over the four samples. With a few exceptions, at the lowest-T values, fluctuation $\delta\rho/\rho$ is generally less than 2%. Hg1201 was solved at $N_\omega = 2^{12}$ and $N_k = 92$, which we have estimated to be sufficiently accurate given the significantly smaller t value.

Also as in [7], theoretical resistivities extending below $T/t = 77.8$ K/eV are found by extrapolating from a fit $\rho \sim \alpha\frac{T^2}{T+T_0}$.

II. Bi2201 RESULTS

A. Fermi surface and band parameters of Bi2201

We study Bi2201 using the following tight-binding parameters:

$$t' = -0.4t, t'' = 0.0, J = 0.17t,$$
$$t = 1.176\,\mathrm{eV}, \quad (10)$$
$$c_L, c_0 = 24.6, 12.3\,\text{Å}\ [13],$$

where the magnitude of t is estimated from a best fit with the resistivity over all available samples, as discussed below in Fig. 2. Our choice in Eq. (10) is guided by requiring the simplest parametrization, with the smallest number of nonzero hopping elements, and differs somewhat from other schemes in the literature. The band parameters suggested in [13], upon

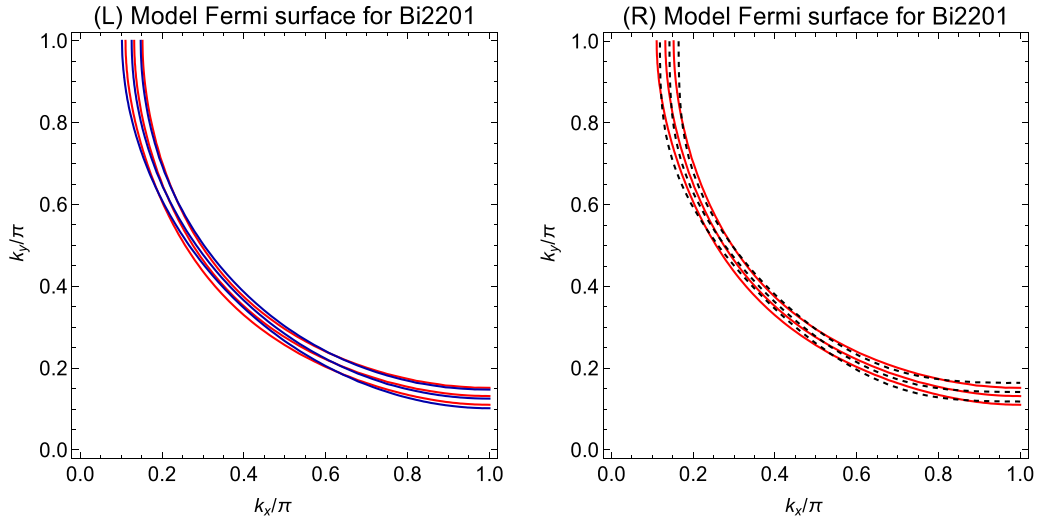

FIG. 1. The band parameters used here are given in Eq. (10). The resulting Fermi surfaces at densities $n = 0.75, 0.8, 0.85$ are shown in red in the two figures and compared to those from other suggested models, with parameters $t'/t = -0.3143$, $t''/t = 0.04286$ (in blue) quoted in [13] (left) and with parameters $t'/t = -0.156$, $t''/t = 0.164$ (dashed lines) quoted in [24] (right).

conversion to the convention used here, are expressible in the form $t' = -0.3143\,t$, $t'' = 0.04286\,t$, and earlier estimates from band theory [24] are farther away, $t' = -0.156\,t$, $t'' = 0.164\,t$. Figure 1 shows that both of these alternate schemes lead to very similar Fermi surfaces found from Eq. (10). While t'/t and t''/t are obtainable from the measured Fermi surface when available, the magnitude of t remains undetermined by these considerations. The magnitude of the single theoretical

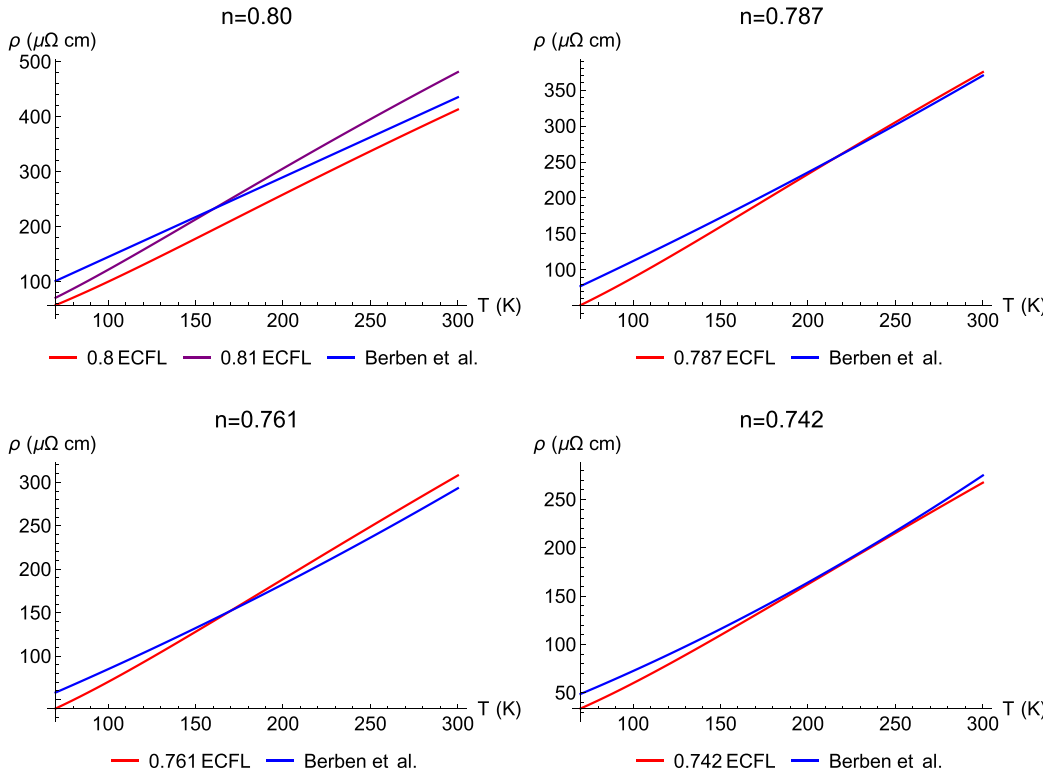

FIG. 2. Bi2201 comparisons. From top left, the ECFL resistivities (in red and magenta) at $n = 0.80$ and 0.81, then (in red) at $n = 0.787, 0.761, 0.742$ plotted against the resistivity data of Berben *et al.* [13] for samples S:4, S:3, S:2, and S:1, respectively. The experimental data have been adjusted for impurity contribution by a simple shift in each case. The top left panel shows the theoretical ECFL resistivities at $n = 0.81$ ($x = 0.19$) as well as $n = 0.8$ ($x = 0.2$), which seems to bracket the data. The ECFL curves use the band parameters in Eq. (10) with $t = 1.176$ eV for all the curves. This value of t seems to be reasonable for the overall available data set, and the tight-binding parameters given by Eq. (10) are used in the calculation of all the Bi2201 figures below. For $T \lesssim 70$ K, the ECFL results are parabolic in T.

parameter t is determined to give a good overall fit to the resistivities over available densities, as noted in Fig. 2. We also made a few further checks with the the parametrization in [13], which yielded very similar resistivities after adjusting the scale of t.

We first summarize the available samples from [11–13] in Table I and discuss their resistivity in detail below. Their T_c's and other parameters are listed in Table I. In the last row of Table I, we also include the early measurement of [11,12]. Here we review those early findings in the context of recent and modern measurements in [13], as well as calculations from the ECFL theory.

In [13], the normal-state resistivity of samples S:1–S:4 is reported for temperatures up to 300 K. The question of determining the hole density x in this system is discussed in [13]. They estimate $x(=p)$ by comparing the observed resistivity $\rho(T)$ and $d\rho(T)/dT$ with observations on LSCO at different densities [8]. They observe that for x deduced from different arguments, such as the ARPES Luttinger count, comparing resistivity and its T derivatives and the phenomenological relation [Eq. (14)] between T_c and x lead to rather different results in general. For the samples studied further in this work, we could not find the recommended estimates of x in the paper [13], and therefore used Eq. (14) to arrive at the x column using the quoted T_c values, as detailed in [25]. Since the ECFL calculation—with suitable parameters—leads to a consistent quantitative description of the LSCO resistivity ρ and the derivative $d\rho/dT$ data from [8], we go ahead and compare the current calculation with all the reported resistivity data below, where we evaluate and comment on the quoted x values as well as make suggestions to revise them.

B. Resistivity of Bi2201

In Fig. 2, we compare the ECFL theory resistivity with that from samples S:1–S:4 of [13]. We note that the $d\rho/dT$ of the two sets are close; however, the sample S:4 has somewhat bigger ρ than the theoretical estimate, indicating that the estimated x might be slightly off. For this purpose, the top left panel in Fig. 2 shows the ECFL resistivities at $n = 0.81$ ($x = 0.19$) as well as $n = 0.8$ ($x = 0.2$) with identical remaining parameters, which seem to bracket the experimental result for the sample S:4.

Turning to the data from S:5 [11,12], in Fig. 3 we compare the resistivity with S:1 from [13]. In Table I, we see that by using the phenomenological relation [25,27], these two are expected to be very close, but the resistivities do not appear to be very close. We next compare these with the ECFL resistivities at $n = 0.71, 0.68$ using the previously determined value $t = 1.176$ eV. It seems thus that these two curves bracket the result for S:5. We explore this further by plotting the resistivity over a much bigger T scale, up to 800 K, in Fig. 4. It is seen here that there is a reasonable match between the two curves over most of the range.

In Fig. 5, we display the ECFL resistivities using the band parameters in Eq. (10) over a wide set of densities and a broad range of T. We note that the nonlinear (usually quadratic) corrections to the resistivity become more evident as the particle density n increases, being almost linear over the whole range at the lowest density, as also seen in Fig. 4.

TABLE I. Samples S:1–S:4 of Bi2201 studied in 2022 [13] and sample S:5 studied in 1989 [11,12] are compared with theory. Resistivity measurements are reported up to T_{max}. In [13], the observed T_c for each of these overdoped samples is used to estimate the hole density x using the phenomenological relation given by Eq. (14). The quoted T_c of sample S:5 [11,12] converts to a density $x = 0.259$ by using Eq. (14). This value is essentially identical to that of sample S:1 in [13], but is observed to have a substantially different magnitude of resistivity from it, as seen in Fig. 3. Theoretically (see Fig. 4), $x = 0.32$ seems to be more consistent overall for sample S:5.

Sample No.	Ref.	T_c in K	x Eq. (14)	T_{max} in K
S:1	[13]	7	0.258	300
S:2	[13]	17	0.239	300
S:3	[13]	27	0.213	300
S:4	[13]	31	0.197	300
S:5	[12]	6.5	0.259 (?)	800

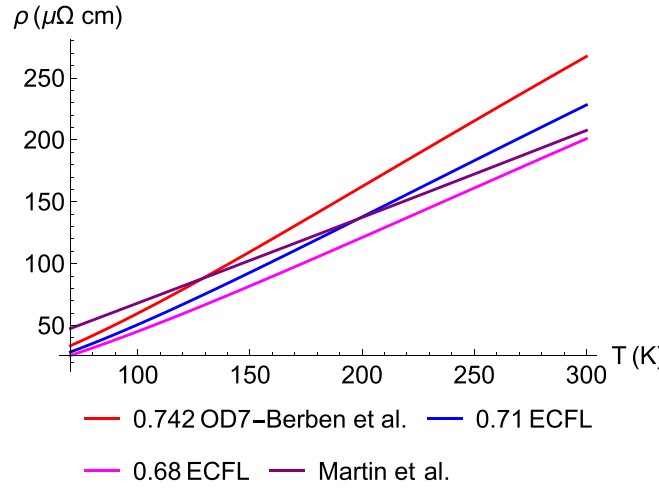

FIG. 3. Bi2201 comparisons. ECFL resistivity at $n = 0.68$ and $n = 0.71$ plotted against the data S:5 from Martin *et al.* [11,12] and S:1 from Berben *et al.* [13].

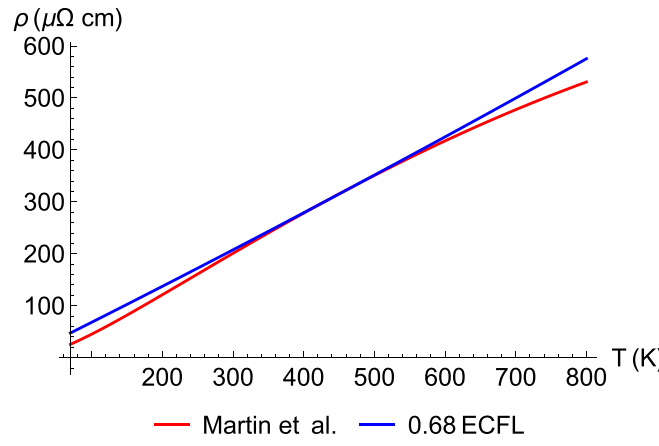

FIG. 4. Bi2201 comparisons. ECFL resistivity at $n = 0.68$ (blue) plotted against the data from Martin *et al.* [11,12] over a wide T range.

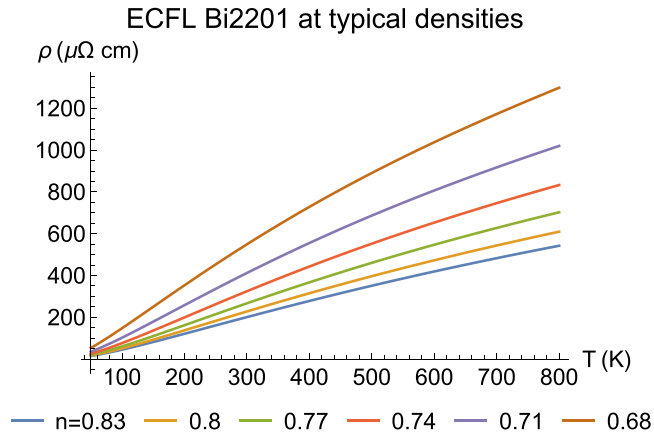

FIG. 5. A summary of ECFL resistivities at typical densities over a wide temperature window.

We also include energy distribution curve (EDC) dispersions sampled in the nodal k direction at our lowest available temperature (91.5 K) in Fig. 6. EDCs are slices of the spectral function across frequency at fixed k. The dispersion shows the ω value at which the spectral peak is found in each k slice plotted against $k - k_F$. A comparison of the dispersion with the band dispersion for the same parameters as shown in the inset gives an estimate of the effective band mass $\frac{m^*}{m}$. See Table II for our effective mass calculations.

III. TL2201 RESULTS

A. Fermi surface and band parameters of Tl2201

The ARPES determined Fermi surface for Tl2201 is available in [14,15]. This work fits it to a band structure:

$$\epsilon(k_x, k_y) = \tfrac{1}{2}\tau_1[\cos(k_x) + \cos(k_y)] + \tau_2 \cos(k_x)\cos(k_y) + \tfrac{1}{2}\tau_3[\cos(2k_x) + \cos(2k_y)] + \tfrac{1}{2}\tau_4[\cos(2k_x)\cos(k_y) + \cos(k_y)\cos(2k_y)] + \tau_5 \cos(2k_x)\cos(2k_y), \quad (11)$$

where, in units of eV, $\tau_1 = -0.725$, $\tau_2 = 0.302$, $\tau_3 = 0.0159$, $\tau_4 = -0.0805$, and $\tau_5 = 0.0034$. Our preference is to use fewer parameters for performing the ECFL calculations

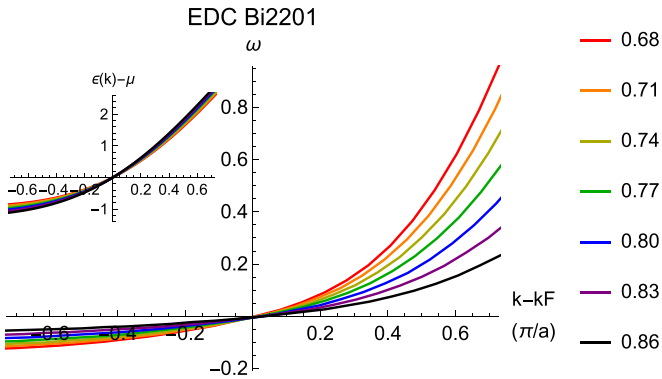

FIG. 6. Bi2201 energy distribution curve (EDC) dispersions across the full range of densities. The inset displays the bare band dispersion minus the chemical potential, $\epsilon(k)-\mu$, in units of t. The ratio of their slopes gives an estimate of the effective masses, which are listed in Table II.

TABLE II. Bi2201 m^*/m defined as the ratio of slopes of $\epsilon(k)$ and the EDC dispersion at $k = k_F$, shown in Fig. 6.

Bi2201							
Density	0.68	0.71	0.74	0.77	0.80	0.83	0.86
m^*/m	7.460	8.462	9.345	10.782	13.291	18.251	23.795

involving a large number of further steps. Hence we checked for the possibility of fitting the Fermi surface resulting from Eq. (11) with, at most, two sets of neighbors, i.e., with t, t', t'' only, and found that there are two distinct types of parameters which provide excellent fits of the above Fermi surface over the full range of studied densities, as seen in Fig. 7. We refer to these as model A and model B. The two hopping variable sets are given by the following for the Tl2201 tight-binding parameters:

$$\begin{aligned} \text{Model A: } & t' = -0.430t, \quad t'' = 0.005t, \\ & t = 1.82\ \text{eV}, \quad J = 0.17t, \\ \text{Model B: } & t' = -0.237t, \quad t'' = 0.138t, \\ & t = 1.053\ \text{eV}, \quad J = 0.17t, \\ & c_L, c_0 = 23.1, 11.56\text{Å}\ [15], \end{aligned} \quad (12)$$

and we included the standard value of J used for easy reference.

We display, in Fig. 7, the Fermi surfaces from Eq. (12) compared with the Fermi surface from Eq. (11).

B. Resistivity of Tl2201

Reference [16] presents the normal-state resistivity of four samples with densities $n = 0.817, 0.773, 0.744, 0.726$. In Figs. 8–10, we compare theoretical resistivities from ECFL for model A and model B for $n = 0.726$, 0.744, and 0.773 to the experimental results from Cooper *et al.* [16]. In general, the resistivities of model A and model B are very close over all densities and temperatures. Figure 11 shows the experimental results for $n = 0.817$. This curve does not agree well with either of our models and seems to be somewhat higher in magnitude. Two higher-density results for model A are displayed for additional comparison; the curve at $n = 0.86$ seems closer in scale to the data. Further data at nearby densities would be helpful to clarify the resistivity-density systematics.

In Fig. 12, we display the full set of results at different densities for model B over a wide range of T; model A gives very similar results and is therefore not displayed.

TABLE III. Tl2201 m^*/m defined as the ratio of slopes of $\epsilon(k)$ and the EDC dispersion at $k = k_F$ shown in Fig. 13.

Tl2201		
Density	Model A m^*/m	Model B m^*/m
0.726	8.056	6.802
0.744	9.386	7.259
0.773	10.854	8.351
0.817	15.443	11.961

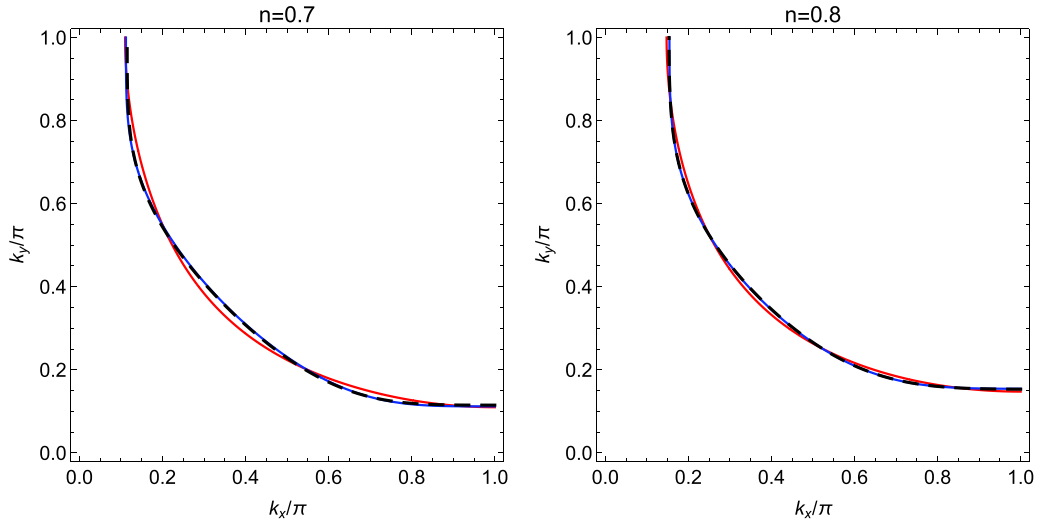

FIG. 7. Left: The Fermi surfaces at $n = 0.7$. The blue curve is from model B [Eq. (12)] and the red curve is from model A [Eq. (12)]. The black dashed line shows the Fermi surface from the experimentally derived energy dispersion in Eq. (11). Right: The same curves at density $n = 0.8$. We thus see that the result from model A is fairly close to the experimentally derived Fermi surface, while model B is nearly exact at these densities.

We also include EDC dispersions sampled in the nodal direction at our lowest available temperatures (141.6 K for model A, 81.9 K for model B) in Fig. 13 for both of our sets of band parameters. Comparison of the dispersion with the band dispersion gives an estimate of the effective band mass $\frac{m^*}{m}$ as shown in Table III. The lowest density, 0.726, has an effective mass of 8.056 in model A and 6.802 in model B. This density is cited in [16] as having the lowest T_c of the set, 26.5 K. In [26], an overdoped Tl2201 sample with a lower T_c (15 K) is referenced as having $m^*/m = 4.1 \pm 1$. Overall, this seems to fit with the pattern observed in our m^*/m calculations, with m^*/m lowering as n (indicated by T_c) decreases.

IV. HG1201 RESULTS

A. Fermi surface and band parameters of Hg1201

ARPES results in [20] provide the following set of tight-binding parameters for Hg1201:

$$t' = -0.228t, \quad t'' = 0.174t, \quad J = 0.17t,$$
$$t = 0.2\ \text{eV},$$
$$c_L, c_0 = 19, 9.5\text{Å}\ [19]. \tag{13}$$

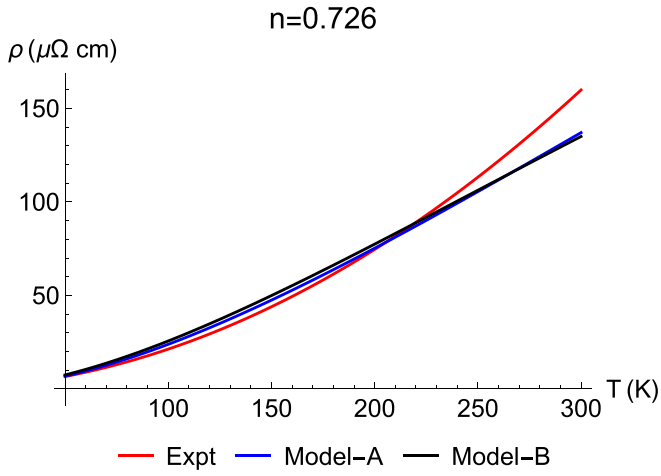

FIG. 8. ECFL resistivity for Tl2201 using parameters in Eq. (12) at a density $n = 0.726$ with model A (blue) and model B (black), compared with the experimental curve from [16]. The two values of t for the two models quoted in Eq. (12) are fixed by fitting the theoretical temperature with the observed one, and are taken to be fixed for other densities. We see that the theoretical curves as well as the experimental one show a significant quadratic correction in T here and at most other densities.

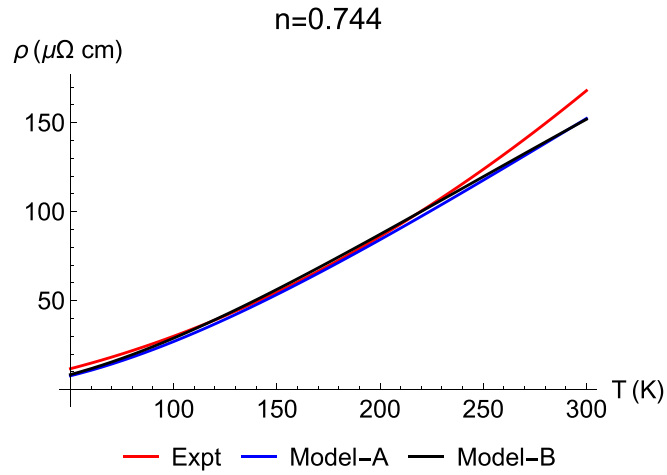

FIG. 9. ECFL resistivity for Tl2201 using parameters in Eq. (12) at a density $n = 0.744$ with model A (blue) and model B (black), compared with the experimental curve from [16]. Below 250 K, the theoretical and experimental curves are seen to be close at this density.

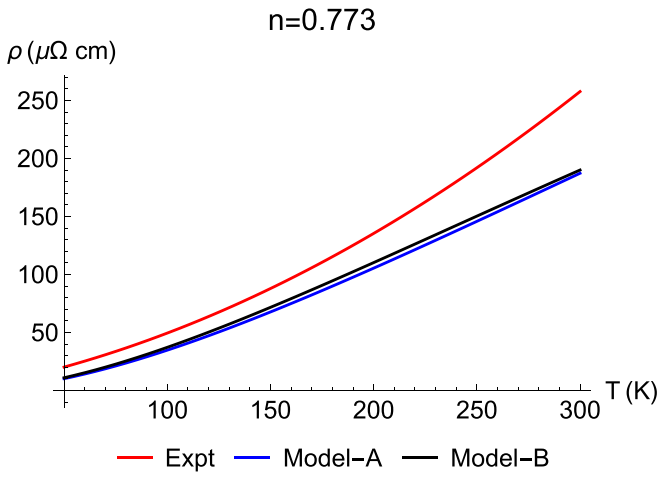

FIG. 10. ECFL resistivity for Tl2201 using parameters in Eq. (12) at a density $n = 0.773$ with model A (blue) and model B (black), compared with the experimental curve from [16]. The experimental curve is somewhat shifted upwards from the theoretical one.

B. Resistivity of Hg1201

The resistivity data for this system are available from Refs. [17,19]. Since the ECFL theory has been developed and tested in the optimum to overdoped regimes, we focus on data within this regime. Reference [17] provides resistivity for samples with a wide range of explicitly stated dopings. Among these, we focus on the four resistivities spanning $n = 0.792$–0.873, in the optimum to overdoped regimes. This range overlaps with the range studied in our other materials. Data were taken from plots in [17] using the data extraction tool DigitizeIt [28]. From the data, an impurity resistivity contribution was estimated and subtracted off for our comparison

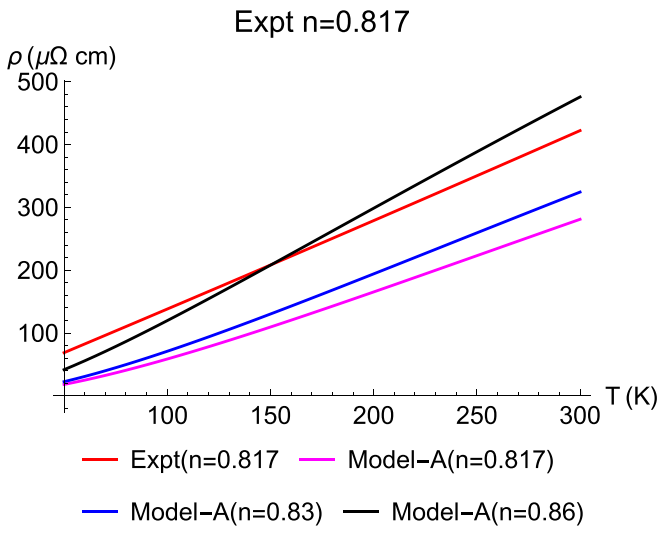

FIG. 11. ECFL resistivity for Tl2201 using parameters in Eq. (12) at a density $n = 0.83$ (blue) and 0.86 (black) compared with the experimental curve at $n = 0.817$. The two theoretical curves bracket the experimental curve, while the theoretical curve at $n = 0.817$ is noticeably below the data.

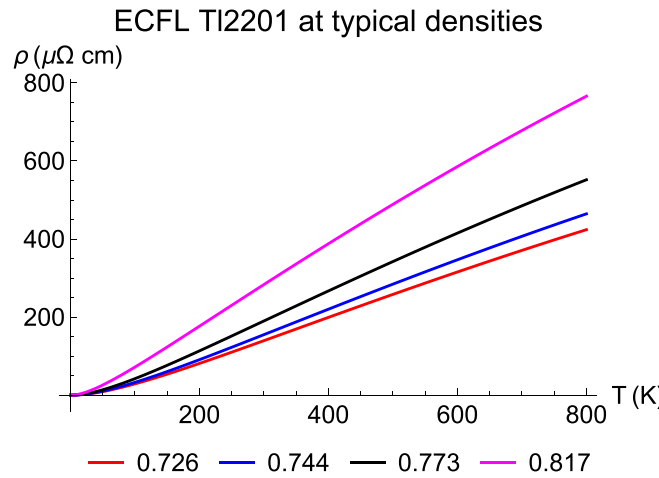

FIG. 12. ECFL resistivities for Tl2201 at typical densities over a larger temperature window using model B.

to theory. Our comparisons between ECFL and experiment are found in Fig. 14.

In common with Bi2201, the electronic density in the Hg1201 material is reported to be too difficult to assign, as compared to other single-layer cuprates. Keeping this in mind, we display, in Fig. 14, the theoretical results at densities quoted in the corresponding experiments [17], and for $n = 0.820$ and $n = 0.873$, at one additional density, somewhat different from the nominal one, where the data match theory somewhat better. While this empirical procedure is suggestive of the origin of the discrepancies, it is not entirely satisfactory from a theoretical perspective.

The full results of ECFL can be seen in Fig. 15.

V. DISCUSSION OF RESULTS

We first comment about a minor difference in the treatment of the impurity contribution to resistivity in this work from that in [7]. In the case of Tl2201, the data for each sample presented in [15,16] are in the convenient form of a fit to a simple function $\rho = \rho_0 + \rho_1 T + \rho_2 T^2$, and hence we drop the term with ρ_0 to compare with theory. We note that for the cases of Bi2201 and Hg1201, we digitized the published data and fit it to a convenient functional form, and followed the same recipe.

Our results for the single-layer compound Bi2201 are compared with theory in Fig. 2. Theory is in reasonable accord *on an absolute scale* with the data from [13] at $n = 0.787$, 0.761, and 0.742. At $n = 0.80$, the theoretical result for $n = 0.80$ is somewhat off from the data, while the result for $n = 0.81$ is close—albeit with a slightly greater slope. There seems to be no single scaling of t which could improve matters at all densities. A notable aspect of the comparison is that the data as well as theory show a T^2 correction to linear behavior of different extent depending on the density.

The density of the sample in [12] was not fixed precisely, as far as we could see. With optimism that might be questionable, we crudely estimated it from the observed T_c, using the phenomenological relation given by Eq. (14) to be $n = 0.74$. This estimate roughly coincides with the density of sample

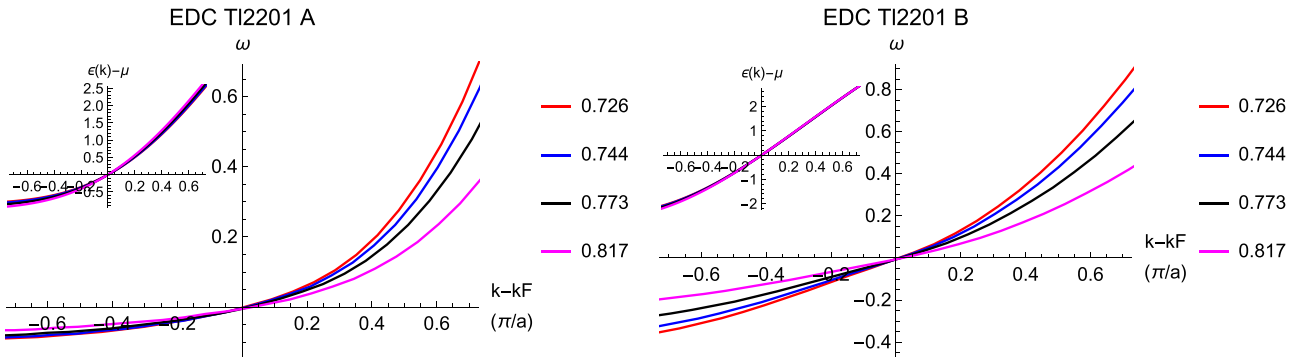

FIG. 13. Tl2201 model A and model B energy distribution curve (EDC) dispersions across all four densities. The inset displays the bare band structure minus the chemical potential, $\epsilon(k)$-μ in units of t. The corresponding effective masses are given in Table III.

S:1 of [13]. In Fig. 3, the data at $n = 0.742$ from [13] and the data from [12] are compared, together with the theoretical curves from ECFL at densities $n = 0.71$ and $n = 0.68$. The theoretical curves are drawn assuming the parameters already determined from the data sets from [13]. These densities are somewhat lower than the theoretical curve at $n = 0.742$ shown in Fig. 2, but seem to bracket the data of [12], suggesting that for some unclear reason, the density of the sample in [12] is close to $n = 0.68$. We take this phenomenological possibility further in Fig. 4 where the theoretical curve at $n = 0.68$ and the data from [12] are compared. Barring the limiting values of T, the match between theory and the data seems intriguing, especially given the broad range of temperatures—up to 800 K.

Turning to Tl2201, in Eqs. (8)–(11), we compare the data at densities $n = 0.726$, 0.744, 0.773, and 0.817 with the theoretical results found using the two band models described in Eq. (12). The two theoretical models start from two rather different sets of parameters characterized by distinct t'/t, t''/t values, and somewhat surprisingly describe the Fermi surface shape almost equally well, as seen in Fig. 7. It is therefore of interest to note that the resistivities of the two models agree very well, after a suitable choice is made of the nearest-neighbor hopping t for each model, and seems to confirm the

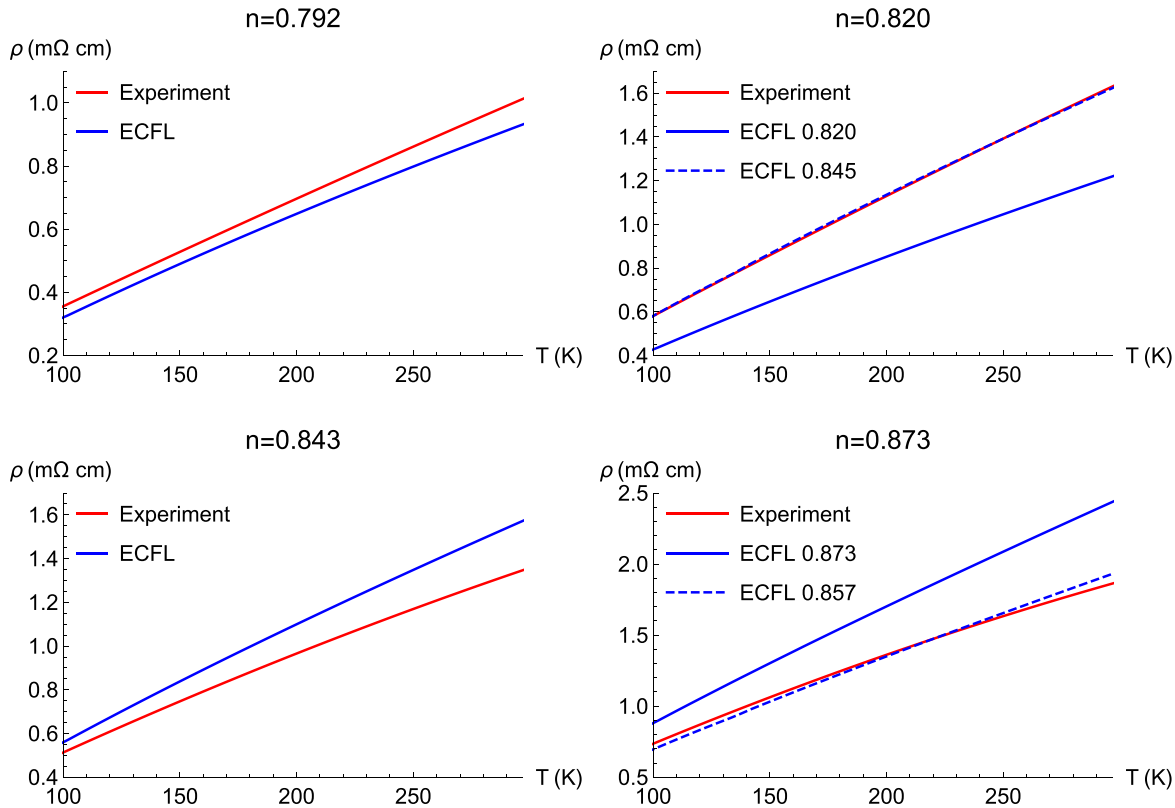

FIG. 14. Hg1201 comparisons: ECFL resistivities (blue) compared to resistivity data from [17] fit down to $T = 0$ with impurity resistivity subtracted. For $n = 0.820$ and 0.873, a second ECFL curve is also displayed as a dashed line, showing a different density that more closely matches the experiment.

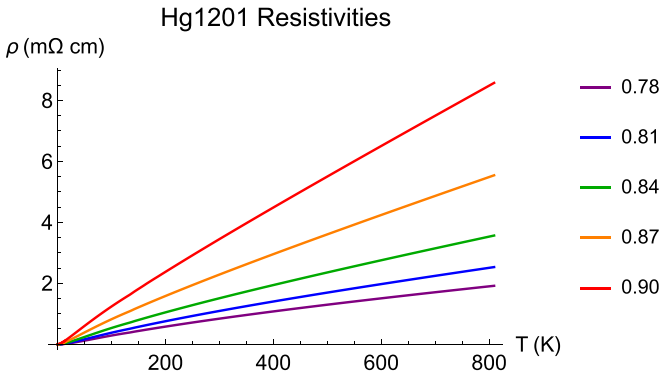

FIG. 15. The full set of ECFL resistivities for Hg1201. Other densities used below are found from an interpolation of these.

initial belief that the Fermi surface shape largely determines the resistivity results. We note that the data for $n = 0.726$ and $n = 0.744$ agree on an absolute scale with theory, whereas at higher densities, $n = 0.773$, the data are parallel but offset from the theoretical curves. At $n = 0.817$, the discrepancy between theory and experiment is greater than at lower densities. To quantify this, we also display the calculated resistivity at $n = 0.83$ and $n = 0.86$ along with $n = 0.817$. It is interesting that the theoretical curve for $n = 0.86$ has the same scale as the experiment, and it might be interesting to obtain data from samples with other densities in this range.

For Hg1201, we have calculated ECFL results for a range of densities as shown in Fig. 15, and we have made interpolations from these curves for comparison to four of the densities ($n = 0.792$, 0.82, 0.843 and 0.873) found in [17], as seen in Fig. 14. The data for $n = 0.792$ and $n = 0.843$ are reasonably close to the theoretical curves, while $n = 0.82$ and $n = 0.873$ theory and data are parallel over this range, but display a vertical shift. For illustrative purposes, we provide alternate densities from the nominal (quoted) ones where the matching is closer.

It might be useful to visualize the full set of theoretical resistivities, and their systematic progression with density and temperature. For this purpose, we display the theoretical resistivities for Bi2201 in Fig. 5 over a broad range of temperatures for six densities. Similarly, theoretical resistivities for Tl2201 model B are provided in Fig. 12, and for Hg1201 in Fig. 15.

VI. CONCLUDING REMARKS

In the present work and our earlier work [7], we have performed a detailed application of the extremely correlated Fermi liquid theory to calculate the normal-state resistivity of single-layer high-T_c cuprate materials in the optimum to overdoped density regimes. The relative simplicity of the single-layer materials compared to other strongly correlated materials arises from the almost decoupled nature of the layers, so that a purely two-dimensional description, ignoring motion in the third direction, is quite reasonable. The ECFL theory requires a very few parameters—detailed in Eq. (8)—and yields resistivity on an absolute scale. Comparing the results with experiments is therefore feasible. It becomes especially meaningful, provided a large enough set of materials and data sets are included. It is of interest to see if the wide variety of experimentally seen behavior—with variable T dependence and nontrivial density dependence—can be reproduced quantitatively by the theory.

With the addition of results for the three systems added here to the systems already studied in [7], we now have a comparison between all available single-layer compounds and the set of results of ECFL. In Table IV, we display the full set of band parameters we deduced to analyze these systems. From a theoretical viewpoint, the qualitative results for the resistivity ρ in ECFL theory can be summarized as follows. We find a $\rho \propto T^2$ behavior at very low $T \ll t/k_B$, crossing over at a low T (still at $T \ll t/k_B$) to $\rho \propto T$ in a "strange metal" regime. This behavior is robustly realized in much of the data. At a quantitative level, given the uncertainties in the determination of material parameters, the comparison between theory and experiments found in our work seems fair. The originally surprising difference in the curvature observed between electron- and hole-doped resistivities is also understandable within the theory, being related to a reversal of sign of the effective second-neighbor hopping t'/t [7]. Studies of the T dependence of the resistivity have the potential of uncovering the nature of the underlying many-body ground states in strongly correlated systems, i.e., to answer the question of whether it is a Fermi liquid state of some sort or a non-Fermi liquid state. The resistivity is inferred from the electronic Green's functions by several steps as in Eq. (9), and is therefore somewhat indirect. In contrast, it has been pointed out recently [29] that a direct answer to the Fermi liquid or non-Fermi liquid question can be found by using the angle-resolved photoemission spectroscopy to experimentally infer the imaginary self-energy of the electron from the spectral intensity near the Fermi wave vector. We hope that these results will provide motivation for carrying out further experiments suggested here.

ACKNOWLEDGMENTS

This work used Expanse by Dell and SDSC through allocation DMR170044 from the Advanced Cyberinfrastructure Coordination Ecosystem: Services and Support (ACCESS) program, which is supported by National Science Foundation Grants No. 2138259, No. 2138286, No. 2138307, No. 2137603, and No. 2138296 [30]. We thank Prof. A. Carrington, Prof. J. R. Cooper, Prof. M. Greven, and an anonymous referee for helpful comments.

DATA AVAILABILITY

The data are openly available [31]. For convenience, we created smaller $N_k = 92$, $N_\omega = 2^{12}$ files from which we fit and stored the spectral data as polynomials. We include this data as supplemental material, along with a Jupyter notebook for processing. This can be used to retrieve a reasonable approximation of our resistivities, to interpolate to new resistivities at different n values, and to perform any other desired calculations with the spectral functions. To make the set of available data comprehensive, we have also included BSLCO and LSCO results.

TABLE IV. For 37 samples belonging to seven families of single-layer cuprates, a comparison of experiments with the ECFL theory is carried out in this work and in [7]. The first five rows consist of the known hole-doped single-layer materials and the last two are the electron-doped single-layer materials. We summarize the range of hole density x (=1–n), the number of samples, and the temperature range studied, in the first three columns. In the last three columns, we list the band parameters used in the theory.

All single-layer cuprate high-T_c materials					
Hole doped	x range ($N_{\rm samp}$)	$T_{\rm max}$(K)	t'/t	t''/t	t (eV)
$La_{2-x}Sr_xCuO_4$ (LSCO) [8]	0.12–0.22 (11)	400	−0.2	0	0.9
$Bi_2Sr_{2-x}La_xCuO_6$ (BSLCO) [8]	0.12–0.18 (7)	300	−0.25	0	1.35
$Bi_2Sr_2CuO_{6+x}$ (Bi2201) [13]	0.213–0.258 (4)	300	−0.4	0	1.176
(Bi2201) [11,12]	0.259–{0.32?} (1)	800	−0.4	0	1.176
$Tl_2Sr_2CuO_{6+x}$ (Tl2201 model A) [16]	0.183–0.274 (4)	300	−0.430	0.005	1.82
(Tl2201 model B) [16]			−0.237	0.138	1.053
$HgBa_2CuO_{4+x}$ (Hg1201) [17]	0.127–0.208 (4)	300	−0.228	0.174	0.22
Electron doped					
$Nd_{2-x}Ce_xCuO_4$ (NCCO) [9]	0.125–0.15 (2)	400	+0.2	0	0.9
$La_{2-x}Ce_xCuO_4$ (LCCO) [10]	0.14–0.17 (4)	300	+0.2	0	0.76

[1] B. S. Shastry, Extremely correlated Fermi liquids:, Phys. Rev. Lett. **107**, 056403 (2011); Extremely correlated Fermi liquids The formalism, Phys. Rev. B **87**, 125124 (2013).

[2] L. D. Landau and I. Y. Pomeranchuk, On the properties of metals at very low temperatures, Sov. J. Expt. Theor. Phys. **7**, 379 (1937).

[3] W. E. Lawrence and J. W. Wilkins, Electron-electron scattering in the transport coefficients of simple metals, Phys. Rev. B **7**, 2317 (1973).

[4] M. J. Rice, Electron-electron scattering in transition metals, Phys. Rev. Lett. **20**, 1439 (1968).

[5] K. Miyake, T. Matsuura, and C. M. Varma, Relation between resistivity and effective mass in heavy-fermion and A-15 compunds, Sol. State. Commun. **71**, 1149 (1989).

[6] P. Mai and B. S. Shastry, Extremely correlated Fermi liquid of t-J model in two dimensions, Phys. Rev. B **98**, 205106 (2018); see Fig. 24 where the variation with J is discussed.

[7] B. S. Shastry and P. Mai, Aspects of the normal state resistivity of cuprate superconductors, Phys. Rev. B **101**, 115121 (2020).

[8] Y. Ando, S. Komiya, K. Segawa, S. Ono, and Y. Kurita, Electronic phase diagram of high-T_c cuprates from a mapping of the in-plane resistivity curvature, Phys. Rev. Lett. **93**, 267001 (2004).

[9] P. K. Mang, S. Larochelle, A. Mehta, O. P. Vajk, A. S. Erickson, L. Lu, W. J. L. Buyers, A. F. Marshall, K. Prokes, and M. Greven, Phase decomposition and chemical inhomogeneity in $Nd_{2-x}Ce_xCuO_{4\pm\delta}$, Phys. Rev. B **70**, 094507 (2004).

[10] T. Sarkar, R. L. Greene, and S. Das Sarma, Anomalous normal-state resistivity in superconducting $La_{2-x}Ce_xCuO_4$: Fermi liquid or strange metal? Phys. Rev. B **98**, 224503 (2018).

[11] A. T. Fiory, S. Martin, R. M. Fleming, L. F. Schneemeyer, J. V. Waszczak, A. F. Hebard, and S. A. Sunshine, Transport, Tunneling, x-ray, and penetration depth studies of superconducting $Bi_{2+x}Sr_{2-y}CuO_{6\pm\delta}$ crystals, Physica C **162–164**, 1195 (1989).

[12] S. Martin, A. T. Fiory, R. M. Fleming, L. F. Schneemeyer, and J. V. Waszczak, Normal-state transport properties of $Bi_{2+x}Sr_{2-y}CuO_{6\pm\delta}$ crystals, Phys. Rev. B **41**, 846 (1990).

[13] M. Berben, S. Smit, C. Duffy, Y.-T. Hsu, L. Bawden, F. Heringa, F. Gerritsen, S. Cassanelli, X. Feng, S. Bron, E. van Heumen, Y. Huang, F. Bertran, T. K. Kim, C. Cacho, A. Carrington, M. S. Golden, and N. E. Hussey, Superconducting dome and pseudogap endpoint in Bi2201, Phys. Rev. Mater. **6**, 044804 (2022).

[14] M. Platé, J. D. F. Mottershead, I. S. Elfimov, D. C. Peets, Ruixing Liang, D. A. Bonn, W. N. Hardy, S. Chiuzbaian, M. Falub, M. Shi, L. Patthey, and A. Damascelli, Fermi surface and quasiparticle excitations of overdoped $Tl_2Ba_2CuO_{6+\delta}$, Phys. Rev. Lett. **95**, 077001 (2005).

[15] C. C. Tam, M. Zhu, J. Ayres, K. Kummer, F. Yakhou-Harris, J. R. Cooper, A. Carrington, and S. Hayden, Charge density waves and Fermi surface reconstruction in the clean overdoped cuprate superconductor $Tl_2Ba_2CuO_{6+\delta}$, Nat. Commun. **13**, 570 (2022).

[16] J. R. Cooper, J. C. Baglo, C. Putzke, and A. Carrington, Thermoelectric power of overdoped Tl2201 crystals: Charge density waves and T^1 and T^2 resistivities, Supercond. Sci. Technol. **37**, 015017 (2024).

[17] A. Yamamoto, W. Hu, and S. Tajima, Thermoelectric power and resistivity of $HgBa_2CuO_{4+\delta}$ over a wide doping range, Phys. Rev. B **63**, 024504 (2000).

[18] A. Tokiwa-Yamamoto, K. Isawa, M. Itoh, S. Adachi, and H. Yamauchi, Composition, crystal structure and superconducting properties of Hg-Ba-Cu-O and Hg-Ba-Ca-Cu-O superconductors, Physicia C **216**, 250 (1993).

[19] N. Barišić, M. K. Chan, Yuan Li, Guichuan Yu, Xudong Zhao, M. Dressel, A. Smontara, and M. Greven, Universal sheet resistance and revised phase diagram of the cuprate high-temperature superconductors, Proc. Natl. Acad. Sci. USA **110**, 12235 (2013).

[20] I. M. Vishik, N. Barisic, M. K. Chan, Y. Li, D. D. Xia, G. Yu, X. Zhao, W. S. Lee, W. Meevasana, T. P. Devereaux, M. Greven, and Z.-X. Shen, Angle-resolved photoemission spectroscopy study of $HgBa_2CuO_{4+\delta}$, Phys. Rev. B **89**, 195141 (2014).

[21] T. Das, Q=0 collective modes originating from the low-lying Hg-O band in superconducting $HgBa_2CuO_{4+\delta}$, Phys. Rev. B **86**, 054518 (2012).

[22] D. Pelc, M. J. Veit, C. J. Dorow, Y. Ge, N. Barisic, and M. Greven, Resistivity phase diagram of cuprates revisited, Phys. Rev. B **102**, 075114 (2020).

[23] M. Ogata and H. Fukuyama, The t-J model for the oxide high-Tc superconductors, Rep. Prog. Phys. **71**, 036501 (2008).

[24] P. Mistark, H. Hafiz, R. S. Markiewicz, and A. Bansil, Fermi-surface-free superconductivity in underdoped (Bi, Pb)(Sr, La)$_2$Cu O$_{6+\delta}$ (Bi2201), Sci. Rep. **5**, 9739 (2015).

[25] For data from the Bi2201 family, the method adopted here for converting T_c to x following [13] is as follows: The samples are located on the T_c-x parabolic plot assumed to be of the form given by Eq. (14) [27]. This phenomenological relation relates the hole doping x to the transition temperature T_c through

$$x = 0.16 \pm 0.11 \left\{ 1 - \frac{T_c}{T_c^{\mathrm{Max}}} \right\}^{\frac{1}{2}}. \tag{14}$$

Here, the system-dependent T_c^{Max} is taken to be $\sim$35 K, and yields a superconducting dome in the (hole) density range $0.05 \leqslant x \leqslant 0.27$, with an optimal value $x_{\mathrm{opt}} = 0.16$.

[26] B. Vignolle, A. Carrington, R. A. Cooper, M. M. J. French, A. P. Mackenzie, C. Jaudet, D. Vignolles, C. Proust, and N. E. Hussey, Quantum oscillations in an overdoped high-T_c superconductor, Nature (London) **455**, 952 (2008).

[27] M. R. Presland, J. L. Tallon, R. G. Buckley, R. S. Liu, and N. E. Flower, General trends in oxygen stoichiometry effects on T_c in Bi and Tl superconductors, Physica C **176**, 95 (1991).

[28] I. Bormann, DigitizeIt (version 2.0), http://www.digitizeit.de.

[29] B. S. Shastry, Method for reconstructing the self-energy from the spectral function, Phys. Rev. B **110**, 155149 (2024).

[30] T. J. Boerner, S. Deems, T. R. Furlani, S. L. Knuth, and J. Towns, *ACCESS: Advancing Innovation: NSF's Advanced Cyberinfrastructure Coordination Ecosystem: Services & Support* (PEARC, 2023), pp. 173–176.

[31] S. Shears, M. Arciniaga, and B. S. Shastry, Aspects of the normal state resistivity of cuprate superconductors Bi2201, Tl2201, and Hg1201 (Data set) Zenodo (2025), https://doi.org/10.5281/zenodo.15306960.